small structures
www.small-structures.com

Structural and Optical Properties of a 0D Lead Iodide Hybrid Perovskitoid with Aromatic Diammonium Cations

Lucía Olano-Vegas, Pavlo Solokha, Antonella Cutrupi, Davide Spirito, Sergio Marras, Marco Gobbi, Fèlix Casanova, Ferry Prins, Serena De Negri, Luis E. Hueso, and Beatriz Martín-García**

0D hybrid organic–inorganic perovskitoids (HOIPs) are promising candidates for optoelectronic applications, due to the properties arising from the isolation of the metal halide octahedra, such as broadband photoluminescence (PL) emission, ambient stability, and reduced ion migration. However, a better understanding of the role of the organic cation in the crystal phase formed and resulting optical properties is needed, particularly regarding the appearance of anisotropy in the arrangement of the octahedra in the lattice. Here, the synthesis, crystal structure, and optical, vibrational, and electrical properties of a new 0D lead iodide HOIP containing 3-(aminomethyl)pyridinium, 3AMPy, as organic cation, are presented. X-ray diffraction reveals that $3AMPy_2PbI_6$ has an orthorhombic crystal structure consisting of isolated $[PbI_6]^{4-}$ octahedra. Polarization-dependent Raman spectroscopy and optical microscopy reveal narrow modes with preferential crystal orientation and birefringence, respectively. $3AMPy_2PbI_6$ exhibits an isotropic red broadband PL emission shifted to longer wavelengths compared to the 2D and 3D AMPy-PbI_2 phases and to other 0D Pb-based HOIPs, which is ascribed to exciton recombination and trap states in the octahedra. Devices made with flakes of $3AMPy_2PbI_6$ show photoconduction under 405 nm light. Our results provide insight into the structure and optical properties of 0D HOIPs and their potential in optoelectronic devices.

1. Introduction

Hybrid organic–inorganic metal-halide perovskites are compounds that combine organic cations and inorganic networks formed by different arrangements of $[BX_6]^{4-}$ octahedra, where B is a metal cation and X is a halogen anion. Their hybrid organic–inorganic nature provides a versatile platform for creating materials with on-demand optical, electrical, and magnetic properties by varying these compounds' composition and dimensionality. Usually, a 3D arrangement of the octahedra is formed with the general formula $A^{I}B^{II}X_3$, where the A site is occupied by small organic molecules, usually ammonium cations. Regarding the dimensionality of perovskites, it is defined as the number of spatial directions in which the $[BX_6]^{4-}$ octahedra are connected. It can vary between 3D, 2D, and 1D to 0D depending on the size of the cations at the A sites. Larger cations cause a reduction in dimensionality, "breaking" a 3D perovskite structure into a 2D, 1D, or 0D structure.[1–4] We note that

L. Olano-Vegas, F. Casanova, L. E. Hueso, B. Martín-García
CIC nanoGUNE BRTA
Donostia-San Sebastián, 20018 Basque Country, Spain
E-mail: l.hueso@nanogune.eu; b.martingarcia@nanogune.eu

L. Olano-Vegas
Departamento de Polímeros y Materiales Avanzados: Física, Química y Tecnología
University of the Basque Country (UPV/EHU)
Donostia-San Sebastian, 20018 Basque Country, Spain

P. Solokha, S. De Negri
Dipartimento di Chimica e Chimica Industriale
Università degli Studi di Genova
16146 Genova, Italy

The ORCID identification number(s) for the author(s) of this article can be found under https://doi.org/10.1002/sstr.202500227.

DOI: 10.1002/sstr.202500227

A. Cutrupi, F. Prins
Condensed Matter Physics Center (IFIMAC)
Autonomous University of Madrid
28049 Madrid, Spain

A. Cutrupi, F. Prins
Department of Condensed Matter Physics
Autonomous University of Madrid
28049 Madrid, Spain

D. Spirito
BCMaterials - Basque Center for Materials, Applications, and Nanostructures
UPV/EHU Science Park, Leioa, 48940 Basque Country, Spain

S. Marras
Materials Characterization Facility
Istituto Italiano di Tecnologia
16163 Genova, Italy

M. Gobbi
Materials Physics Center CSIC-UPV/EHU
Donostia-San Sebastián, 20018 Basque Country, Spain

the resulting 1D and 0D crystals should be referred to as perovskitoids, since, strictly speaking, they do not possess a perovskite structure.[5,6]

0D hybrid organic–inorganic perovskitoids (HOIPs) have recently attracted significant attention due to their exceptional optical and electronic properties.[3,7–11] Unlike their 3D, 2D, and 1D counterparts, 0D HOIPs consist of spatially isolated $[BX_6]^{4-}$ octahedra separated by organic cations and lacking direct electronic coupling with neighboring octahedra.[7,12] This structural change from 3D to 0D leads to distinct quantum effects, such as high exciton binding energies of several hundred meV, substantially higher than those of their 3D counterparts;[13] strong electron-phonon coupling and a soft lattice structure, leading to self-trapped excitons (STEs); and broadband photoluminescence (PL) emission with large Stokes shift[14–16] and a high PL quantum yield.[5,17] These features make them particularly attractive as materials for light-emitting diodes (LEDs).[3,18,19] Another interesting property of 0D HOIPs is their structural tunability. The choice of organic cation plays a crucial role in determining not only their optical and electronic properties but also their stability under ambient conditions.[12] The incorporation of aromatic spacers, for instance, improves their structural stability under moisture and heat, and reduces ion migration with respect to that of conventional 3D perovskites, addressing one of the major limitations of metal halide perovskites in device applications.[3,20,21] Therefore, 0D HOIPs have been proposed as promising candidates in mixed-dimensional heterojunction perovskite solar cells to increase device stability and durability without losing efficiency.[8,22] However, there are still open questions to be addressed before the structural versatility of these materials can be fully exploited. One of these relates to the role of the A site cation, which influences the arrangement and tilting of the $[BX_6]^{4-}$ octahedra and therefore restricts the compounds that can form and their resultant optical properties.[10,19] Another question refers to the emergence of anisotropy in the whole crystal lattice, affecting the properties (e.g., vibrational or optical) of the material and broadening the range of applications.[7,23]

A very suitable choice of material to investigate these questions is that of Pb-based HOIPs, well-known for their excellent optoelectronic performance,[1,8,24–27] combined with aromatic diammonium cations, which provide effective isolation for the metal halide units in 0D structures,[12,14] while maintaining the material's inherent structural rigidity and stability.[28] In this work, we study the structural, vibrational, optical, and electrical properties of (3-(aminomethyl)pyridinium)$_2PbI_6$ ($3AMPy_2PbI_6$) bulk crystals and mechanically exfoliated flakes to elucidate its anisotropic properties, as well as the confinement of excitons and carriers in the metal halide lattice. X-ray diffraction (XRD) studies reveal that the synthesized crystals represent a new phase of the 3AMPy-PbI_2 family, concretely a 0D HOIP instead of the previously reported 2D[29] and 3D[5] crystal structures. Polarization-dependent Raman spectroscopy and optical microscopy reveal the presence of modes with a preferential orientation and birefringence, respectively. By contrast, the PL emission does not show evident polarization dependence, but, interestingly, it is broader and different than for the 2D $3AMPyPbI_4$[29] and 3D $3AMPyPb_2I_6$[5] phases and other 0D Pb-based HOIPs.[16] Additionally, temperature-dependent and time-resolved PL measurements provide insight into the exciton dynamics. Finally, we evaluate the potential of 0D $3AMPy_2PbI_6$ flakes for optoelectronic applications by fabricating lab-scale photodetectors. Our findings contribute to a broader understanding of 0D HOIPs and their suitability for next-generation optical and electronic devices.

M. Gobbi, F. Casanova, L. E. Hueso, B. Martín-García
IKERBASQUE
Basque Foundation for Science
Bilbao, 48009 Basque Country, Spain

2. Results and Discussion

Bulk crystals were synthesized in HI medium using a chemical route slightly different than the one previously reported for 2D $3AMPyPbI_4$[29] and 3D $3AMPyPb_2I_6$[5] phases. Specifically, we used 1:1 molar ratio 3AMPy:Pb, PbI_2 as Pb source, no H_3PO_2 was added, and no intermediate thermalization steps were used during the process of boiling, dissolving, and cooling down to induce crystallization (see Experimental section and Table S1, Supporting Information). In this way, we obtained orange-yellowish single crystals of tens and hundreds of μm size (**Figure 1**a,b), which have an axis of preferential growth (Figure 1b,c). To assess the crystal structure of the compound, we performed XRD measurements on powders and single crystals at room temperature (Figure 1d). The refined crystal structure, with very good residual parameters, shows that $3AMPy_2PbI_6$ crystallizes in the orthorhombic space group *Pbca* (no. 61) with lattice parameters a = 16.7196(5) Å, b = 8.4960(2) Å, and c = 17.7782(5) Å [CSD-2 374 339] (Figure 1e, VESTA[30] visualization). Moreover, temperature-dependent single-crystal XRD data show that this HOIP is stable, and it retains the same crystal structure across the 100–373 K temperature range. Cell volume and anisotropic thermal displacement parameters linearly decrease when cooling down, while atomic positions change only slightly (see Figure 1g and SI.cif files). The synthesized crystals correspond to a 0D HOIP composed of isolated $[PbI_6]^{4-}$ octahedra, which, from a structural point of view, differs from their arrangement in the 2D and 3D phases reported in literature,[5,29] demonstrating that at least three 3AMPy-Pb-I different crystal phases can be obtained by changing crystal growth conditions, the ratios of precursors and Pb source.

Moreover, the 0D $3AMPy_2PbI_6$ bulk crystals can be mechanically exfoliated to obtain flakes with tens of μm size (Figure 1c) and thickness in the range 1–2 μm, which can be transferred onto target substrates by deterministic dry-transfer[31] (see Experimental section). More interestingly, by XRD characterization, we confirm that the obtained flakes are oriented on the (00*l*) plane (Figure 1h).

To gain more insight into the crystal structure, we performed Raman spectroscopy measurements on crystals and flakes at room temperature. The corresponding Raman spectra show more than 30 modes (**Figure 2**a). The peaks at the low-frequency region ($<200\,cm^{-1}$) mostly correspond to vibrations of the inorganic $[PbI_6]^{4-}$ octahedra,[16,32] while the higher frequency modes ($>200\,cm^{-1}$) originate from vibrations of the organic 3AMPy cations.[33] The full-width-at-half-maximum (FWHM) of these $[PbI_6]^{4-}$ octahedra modes ranges between 4 and $10\,cm^{-1}$.

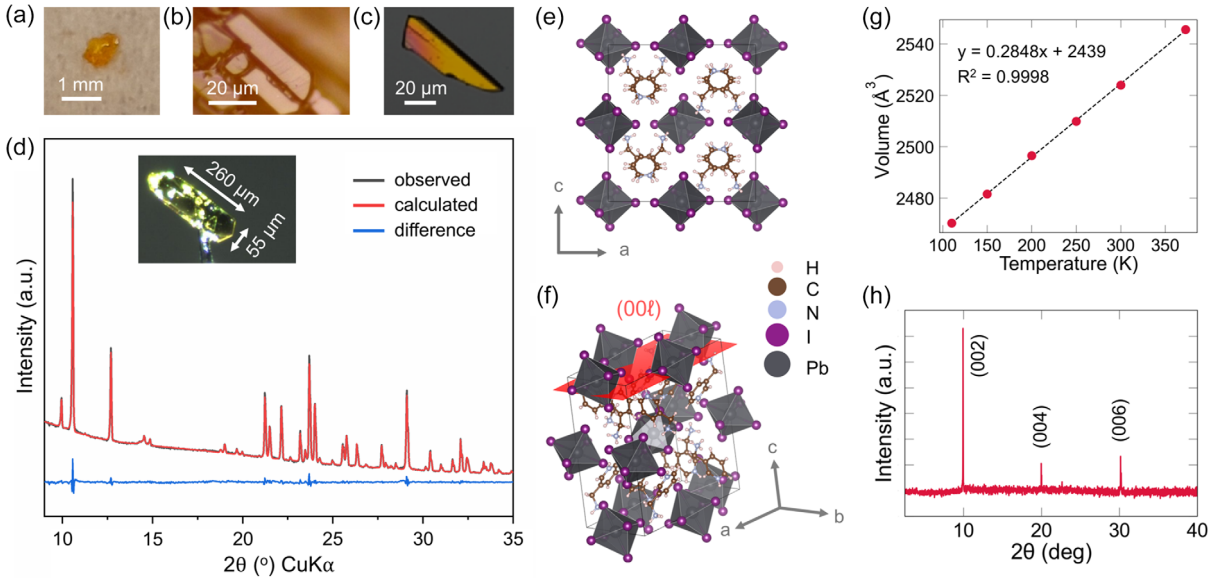

Figure 1. a) Photograph of a $3AMPy_2PbI_6$ crystal. b) Optical image of a single crystal. c) Optical image of a flake on a Si/SiO_2 substrate. d) Result of the fitting carried out on the X-ray powder diffraction pattern, showing the observed and the calculated curves, as well as their difference. Inset: photograph of a representative single crystal selected for X-ray measurements. e) Visualization of the crystal structure down the *b*-axis, showing the inorganic octahedra and the 3AMPy organic spacer. f) Visualization of the crystal structure from another perspective, highlighting the (00*l*) plane. g) Cell volume as a function of temperature. h) XRD pattern of a crystal, showing the exfoliation in the (00*l*) plane marked in red in panel f.

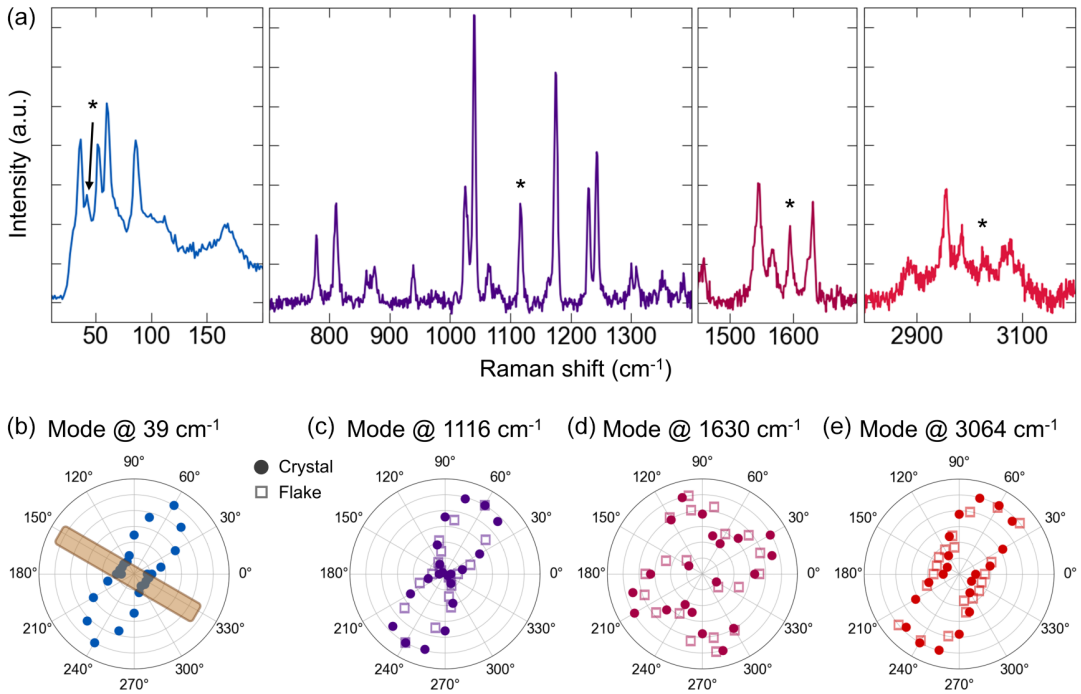

Figure 2. a) Representative Raman spectrum of a $3AMPy_2PbI_6$ crystal showing the different ranges under study. The angle-dependence intensity of the peaks within each of these regions shows a distinctive behavior, as seen in the normalized polar plots b–e), which show a mode representative example for each zone. The analyzed peaks are pointed out with a star in the Raman spectrum panels. The drawing of the flake in b) denotes the angle zero position of the sample. Polar plots c–e) show a comparison between the angle dependent intensity of selected modes for a crystal (full dots) and a flake (empty squares). In both cases, the polar plots have the same orientation.

While sharp vibrations are usually observed coming from aromatic cations in hybrid metal halides,[32,34] Raman modes ascribed to the $[PbI_6]^{4-}$ octahedra are usually broad in 3D[5,35] and 2D[36,37] hybrid lead halides and associated to high anharmonicity. Thus, the narrow peaks we observe stand out and is in accordance with previous reports in 0D Pb-based HOIPs.[16] As the nature of the broadening of Raman modes is currently under scrutiny, with multiple factors including dynamic disorder originating from A-cations, octahedral tilting, or broadening associated to Bose-Einstein statistics,[38] the 0D HOIPs can be a good platform for further studies.

To understand the anisotropy of these vibrations, we carried out angle-resolved linearly polarized Raman spectroscopy measurements by rotating the sample under fixed configuration of polarizer and analyzer parallel to each other (parallel configuration, see Figure S2, Supporting Information and Experimental section for details on the setup). We observed that several modes show a clear modulation of their intensity as a function of the angle of rotation of the sample, highlighted in the polar plots, throughout the entire Raman spectrum (Figure 2b–e).

In the low-frequency region where modes from the inorganic lattice dominate, the angular modulation has a preferential orientation with respect to the long axis of the sample corresponding to the preferential crystal growth direction. The mode centered at 85 cm^{-1} (all modes are detailed in Figure S3, Supporting Information) shows a maximum intensity along the crystal axis, whereas modes centered at 39 cm^{-1} (Figure 2b), 58 cm^{-1}, and 100 cm^{-1} are oriented perpendicular to it. Conversely, the modes centered at 51 cm^{-1} and 112 cm^{-1} seem to display a four-lobe tendency rotated by 45° relative to the crystal axis. The mode centered at 39 cm^{-1} is likely a librational mode of the $[PbX_6]^{4-}$ octahedra, while those at 51 cm^{-1}, 58 cm^{-1}, and 85 cm^{-1} correspond to symmetric bending, and the modes at 100 cm^{-1} and 112 cm^{-1} are associated with stretching.[16]

Modes located in the region 700–1400 cm^{-1} (all modes are detailed in Figure S4, Supporting Information) show two-lobe polar plots oriented perpendicular to the axis of the crystal, being Figure 2c a representative example. This region likely corresponds to C—C, C═C and C—N vibrations such as bending, stretching, or twisting.[34,39,40] The shape of the polar plots changes in the region between 1500 and 1700 cm^{-1} (Figure 2d and Figure S5, Supporting Information), associated with NH_3 bending and scissoring, and C═C stretching in the Py ring.[33] Here, modes at 1546 cm^{-1} and 1595 cm^{-1} show a slight anisotropy aligned with the preferential growth axis of the sample, while mode at 1566 cm^{-1} looks perpendicular and mode at 1630 cm^{-1} seems to display four lobes oriented at 45° with respect to the sample. The polar plots recover their two-lobe shape oriented parallel to the crystal axis in the region 2800–3200 cm^{-1} (Figure 2e and Figure S6, Supporting Information), which in other hybrid perovskites is associated with vibrations of the aromatic ring of the organic cation.

From XRD studies (Figure 1g), we know that flakes are oriented on the *(00l)* plane when exfoliated. We therefore compared the shape of the polar plots for angle-resolved polarized Raman intensity between crystals and flakes (Figure 2c–e), and we observed a perfect match on the intensity modulation with the orientation with respect to the axis of preferential crystal growth indicated in Figure 1b. As a result, we can reliably determine the crystallographic axis of $3AMPy_2PbI_6$ samples of any thickness by angle-resolved linearly polarized Raman spectroscopy, using the parallel configuration, in those modes showing two-lobe polar plots perpendicular to the samples, namely appearing in the 30–150 cm^{-1}, 700–1400 cm^{-1}, and 2800–3200 cm^{-1} ranges.

To study the optical anisotropy of $3AMPy_2PbI_6$, we used polarization-resolved optical microscopy of μm-thick flakes. For this purpose, we used an optical microscope with fixed linearly polarized light at the incidence (IN), and another linear polarizer (analyzer) at the collection path (OUT), with tunable angle from 0° (aligned with the IN polarizer) to 180°. The sample was fixed on the stage of the microscope in two different orientations, namely at angles at which the crystal axis and the IN polarization are different from and equal to 0°, 90°, or their multiples, respectively. The apparent color of the flake is the result of thin film interference due to the thickness of the flake and the Si/SiO_2 substrate, and therefore regions of different thickness appear with different colors. These colors depend on the orientation of the flake to the polarization direction and on the respective alignment (parallel or perpendicular) of the polarizer and the analyzer. When the sample axis is not at 0° (parallel to the IN polarization) nor at 90° (perpendicular to the IN polarization) (**Figure 3**b), we can observe a progressive change of color as the OUT polarizer is rotated from 0° to 90°, recovering the initial color at 180°. On the contrary, when the crystal axis of the sample

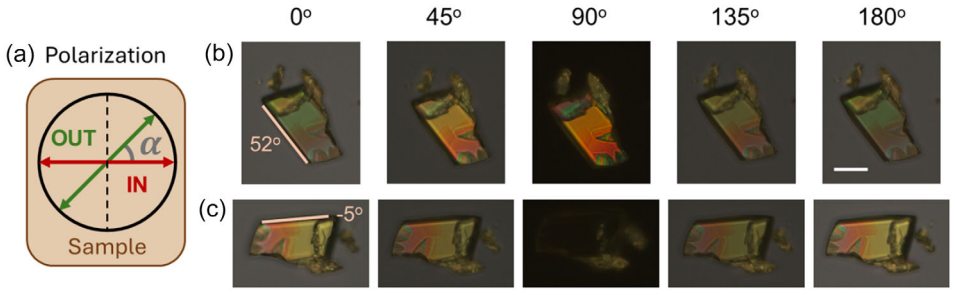

Figure 3. a) Polarization configuration used for taking the optical images. The polarization of the excitation light (IN) is fixed horizontally and sets the zero-degree reference. The sample is fixed and the polarizer at the collection path (OUT) is rotated. b) Optical images of a $3AMPy_2PbI_6$ flake (≈3 μm thickness) oriented at an angle different from 0° or 90° with respect to the input polarization. Each picture is taken at a different angle of the output polarization. A clear change of color is observed as the polarization is rotated. c) Optical images of a $3AMPy_2PbI_6$ flake aligned (±5°) with the input polarization. In this case the flake follows the isotropic behavior of the substrate and blacks out at cross configuration. The scale bar is 15 μm.

is roughly parallel to the IN polarization (Figure 3c), only a change of light intensity is observed, which is due to the polarizers progressively acquiring a cross configuration of their fast axis. The same behavior is observed when the crystal is perpendicular to the IN polarization (Figure S7, Supporting Information). By rotating the sample under the microscope with a piezoelectric motorized stage, we observed that the samples black out approximately at ±10° from the parallel or perpendicular orientation with respect to the IN polarization, while the change of color is maximum at 45°. This optical anisotropy is originating from birefringence,[41] due to the biaxial orthorhombic crystal structure. The light incident on the sample at an angle different from the parallel or perpendicular is refracted into two transversal components travelling through the material at different speed, which induces a wavelength-dependent phase difference. This leads to interference between the two components when they recombine at the exit of the material, being destructive or constructive for some wavelengths depending on the polarization, thus giving the change of color that we see in the images.[42] On the contrary, when the optical axis is aligned parallel or perpendicular to the IN polarization, the incident light does not split into two components, behaving as an isotropic material. Likewise, seeing no difference in color when the crystal is oriented parallel or perpendicular to the IN polarization excludes linear dichroism as the origin of optical anisotropy in this material, since this effect arises when there is a different absorption coefficient between these two axis.[43,44]

We also explored the optical and excitonic properties of $3AMPy_2PbI_6$ by performing detailed PL characterization. Excited by a 405 nm laser, bulk crystals and flakes show a broad PL emission centered around 642 nm (**Figure 4**a) with a FWHM of 140 nm at room temperature, which maintains the 50% of its PL emission after 10 days (see Figure S11, Supporting Information for degradation test). This broadband emission is a characteristic feature of STEs, which arise due to strong electron-lattice coupling and lattice distortions in the isolated $[PbI_6]^{4-}$ octahedra.[13,16,45] As mentioned in the introduction, such behavior is commonly observed in 0D HOIPs, where the lack of electronic coupling between octahedra leads to highly localized excitons and broad emission. Interestingly, the PL emission of $3AMPy_2PbI_6$ is redshifted compared to its 2D ($3AMPyPbI_4$, ≈560 nm)[29] and 3D ($3AMPyPb_2I_6$, ≈545 nm)[5] counterparts (see Table S2, Supporting Information for a comparison among the three materials). This systematic shift may be due to a combination of structural reduction from 3D to 0D and the presence of STE, highlighting the impact of structural changes on optical properties. In addition, the PL emission is significantly broader than in the 2D and 3D phases (FWHM = 33 nm and 54 nm, respectively), further supporting the presence of STEs in the 0D structure. These trends highlight how dimensionality governs the excitonic landscape and emission properties in the $3AMPy\text{-}PbI_2$ family. Notably, while blue to green PL emission is more commonly observed in 0D lead halide HOIPs, and red PL emission often requires mixed-A site

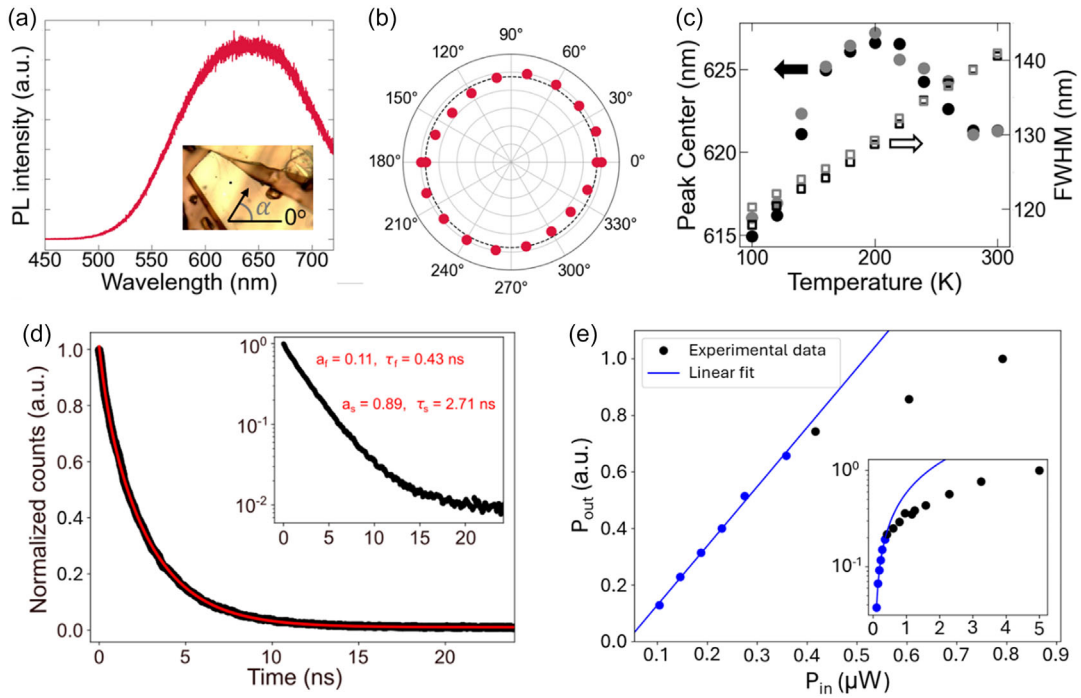

Figure 4. a) Representative PL spectrum of a $3AMPy_2PbI_6$ crystal at room temperature. The inset is an optical image of a crystal. The horizontal line indicates the orientation of the polarization of the excitation light. The sample is rotated and a PL spectrum is recorded every 15°. The normalized intensity is shown in panel b) with the fitting to the mean value. c) Analysis of the peak center (in circles) and FWHM (in squares) of the PL peaks as a function of temperature for two $3AMPy_2PbI_6$ crystals. d) Fluorescence lifetime decay fitted to a biexponential function (solid red line). The inset shows the same data on a semi-logarithmic scale, confirming the multi-exponential behavior of the decay. e) Dependence of the PL (P_{out}) on the excitation power (P_{in}). The low power regime is fitted to a linear function (solid blue line). The inset with a semilogarithmic scale highlights the transition between the low-power and high-power regimes.

cation strategies (Table S3, Supporting Information), here we show red PL emission achieved with a single aromatic diammonium cation.[16] This makes our results particularly noteworthy and underlines the critical role of A-site cation selection in tuning the optical response.[16]

We checked the angle dependence of the PL intensity as the sample is rotated under illumination with a fixed linear polarization at 0° (inset of Figure 4a), and different polarization configurations at the collection path, namely unpolarized, parallel, and perpendicular to the incident polarization. In all the cases, the PL intensity is isotropic (Figure 4b), meaning that exciton emission does not depend on the crystallographic orientation of the material. The isotropic nature of the emission is consistent with the 0D structure, where the isolated octahedra lack directional electronic coupling.

Temperature has, instead, a significant effect on the PL properties (Figure 4c and Figure S8, Supporting Information). The FWHM of the emission increases with increasing temperature, while the PL intensity decreases. On the other hand, the PL emission peak shifts slightly to longer wavelengths as the temperature increases from 100 K, reaching a maximum at 200 K. Above this temperature, the peak shifts back to shorter wavelengths. The shift below 200 K can be explained by the usual temperature behavior of STEs. At low temperature, the STEs are strongly localized. However, as the temperature increases, thermal energy reduces the confinement, leading to a lower-energy emission.[13,45,46] The slight structural changes in the moieties at 200 K (Figure S1, Supporting Information) suggest that the lattice distortions may partially relax at higher temperatures, allowing STEs to emit at slightly higher energies above 200 K.[13,17,45,47]

To further investigate the excitonic behavior, we performed time-resolved PL measurements. The PL decay curve of $3AMPy_2PbI_6$ flakes exhibits a biexponential behavior (Figure 4d), with a fast component ($\tau_1 = 0.43$ ns) related to free exciton recombination and a slower component ($\tau_2 = 2.71$ ns) associated to trap-state or STE emission. Additionally, power-dependent PL measurements indicate the nature of the excited energy carriers (Figure 4e). The PL response scales linearly with excitation power up to ≈1 μW, supporting the exciton recombination as the PL origin. At higher power, the increase is less steep, suggesting the onset of other mechanisms such as Auger recombination that limit the radiative efficiency. As expected for a low-dimensional system, these results confirm the presence of excitonic excited states. Furthermore, to verify the low-dimensional nature of the system, we carried out transient PL microscopy (TPLM) experiments that show a lack of exciton diffusivity (Figure S9, Supporting Information), suggesting highly localized exciton dynamics in this material.

In summary, the non-monotonic temperature dependence of the PL peak, combined with the biexponential decay and power-dependent PL results, suggest the presence of excitonic excited states in $3AMPy_2PbI_6$. The highly localized exciton dynamics, as evidenced by the lack of diffusivity in TPLM experiments, further underscores the 0D nature of the material. These findings highlight the role of STEs in shaping the optical properties of $3AMPy_2PbI_6$. However, other mechanisms may also contribute to the observed redshifted and broadband PL. In particular, the biexponential decay observed in time-resolved PL measurements suggests the presence of trap-assisted recombination pathways, with the slower component likely associated with localized trap states. Additionally, although the octahedral distortion in $3AMPy_2PbI_6$ is relatively low, as is the case of other 0D Pb-based HOIPs (see Table S3, Supporting Information), even subtle distortions can influence the local electronic structure and band edges. Previous studies have shown that such distortions can modulate the density of states and enhance charge localization, contributing to redshifted PL emission.[48] Therefore, while STEs remain the dominant emission mechanism, trap states and minor band structure modifications due to octahedral distortion may also play a synergistic role.

For electrical transport measurements, we exfoliated $3AMPy_2PbI_6$ flakes and transferred them to a n-doped Si/SiO_2 substrate with Pt prepatterned electrodes (**Figure 5**a). We measured these samples under vacuum (10^{-6} hPa) to prevent degradation under ambient atmosphere. As usually the case for HOIPs,[5,49–51] the sample is not conductive under dark conditions. However, it is possible to measure a photo-induced current when the sample is illuminated with a 405 nm laser (Figure 5b, see Figure S10, Supporting Information for white light illumination results), and the intensity of this photocurrent increases with the power of the excitation light. Moreover, to investigate the effect of the light power, as well as the time response of the photocurrent, we measured the drain-source current as a function of time for different powers of the light, under a drain-source voltage of 5 V (Figure 5c). The sample shows a response faster than the experimental resolution of 1 s, which keeps stable in time for powers up to 9.3 μW. When the power is increased above

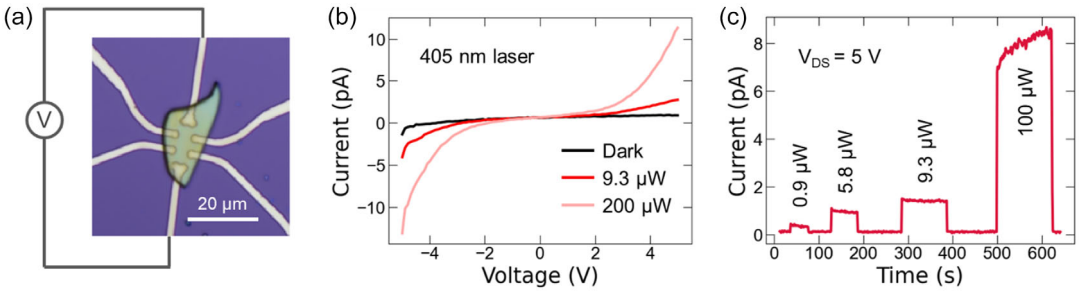

Figure 5. a) Schematics of the device made from an optical image. The $3AMPy_2PbI_6$ flake is stamped on a n-doped Si/SiO_2 substrate with Pt electrodes. b) Output characteristic of the device in dark and under illumination with a 405 nm laser at 9.3 μW and 200 μW respectively. c) Drain-source current on the device under an applied voltage of 5 V and different power of the 405 nm laser.

100 μW, there is a slow increase in the photocurrent following the fast response, which may suggest a heating effect.

3. Conclusion

In this work, we expand the phase diagram of 3AMPy-Pb-I by successfully synthetizing $3AMPy_2PbI_6$ bulk crystals corresponding to a 0D HOIP phase, with an orthorhombic lattice formed by isolated $[PbI_6]^{4-}$ octahedra separated by 3AMPy cations, as confirmed by XRD analysis. This demonstrates the structural versatility of this kind of HOIP materials and the possibility to access different crystal phases by modifying the crystal growth conditions. Temperature-dependent XRD measurements did not reveal any structural phase transitions in the range 100–373 K. Furthermore, Raman spectroscopy measurements demonstrated the presence of narrow modes associated with vibrations of the $[PbI_6]^{4-}$ octahedra. In addition, linearly polarized Raman spectroscopy measurements allowed us to determine the axis of preferential crystal growth, which coincides with the maxima or minima of the angle-dependent intensity of several vibrational modes associated with the inorganic lattice and the organic cation. Regarding the optical properties of $3AMPy_2PbI_6$, we observe the presence of birefringence by polarization-dependent optical microscopy, associated with the two optical axes corresponding to its orthorhombic crystal structure. In contrast, PL emission was found to be isotropic, but most interestingly, it is broader and shifted towards longer wavelengths than the 2D $3AMPyPbI_4$[29] and 3D $3AMPyPb_2I_6$[5] phases or other pure A site cation 0D lead halide HOIPs.[16] This highlights how structural changes and the choice of the A site cation can influence the emission properties. From temperature-dependent PL, time-resolved PL, and TPLM measurements, we can ascribe the observed PL emission to exciton recombination and trap states localized in the octahedra. Furthermore, we integrated mechanically exfoliated flakes into proof-of-concept photodetectors and observed photoconduction under UV and white light illumination. Therefore, our results reveal the potential of these 0D HOIP materials to develop emitters and detectors with on-demand optical properties originating from the presence of isolated octahedra, in a different wavelength range than their corresponding 3D, 2D, or 1D crystal phases. In addition, this study adds a new member to the family of 0D hybrid lead halides and, most importantly, provides a broader understanding of 0D HOIPs' structural, vibrational and optical properties for their future development and applications.

4. Experimental Section

Synthesis of the Bulk Crystals: We mixed 231 mg of PbI_2 (99.999% trace metals basis, perovskite grade) with 2.5 mL of hydroiodic acid (HI, 57% w/w aqueous) in a vial and heated the solution at 240 °C under constant magnetic stirring until dissolution. In another vial placed in an ice bath, we neutralized 52 μL of 3-(aminomethyl)pyridine (3AMPy, 99%) with 500 μL of HI solution. When the mixture PbI_2/HI was dissolved, we incorporated it into the 3AMPy/HI mixture and we heated back at 240 °C and stirred until dissolution. Then, the stirring and heating were stopped, and the solution was left to cool down until crystals appeared. Before reaching room temperature, orange crystals started to form. Then, we quickly isolated the grown crystals by filtration on a Büchner funnel using paper filter (Fisherbrand Grade 111 Cellulose) by vacuum suction and dried inside a vial during at least 8 h at room temperature under reduced pressure using a vacuum pump before being used for the fabrication. All the reagents and solvents were purchased from Sigma Aldrich-Merck and used as received without further purification.

XRD Characterization and Analysis: A translucent intense yellow, plate-shaped crystal was mounted on the goniometer head of a three-circle Bruker D8 QUEST diffractometer equipped with a PHOTON III photon counting detector and with an Oxford Cryostream 1000. The diffractometer used MoK_α radiation ($\lambda = 0.71076$ Å). Complete datasets (four w-scans) were collected at 110, 150, 200, 250, 300, and 373 K over the reciprocal space up to ≈28.3° in θ (corresponding to a ≈0.75 Å resolution) with exposures of 5 s per frame. All data were integrated with SAINT V8.40B;[52] a Multi-Scan absorption correction using SADABS 2016/2 was applied.[53] The structure was solved by the intrinsic phasing method with SHELXT 2018/2 and refined by full-matrix least-squares methods against F^2 using SHELXL-2019/2.[54,55] All nonhydrogen atoms were refined with anisotropic displacement parameters. All C-bound hydrogen atoms were refined isotropic on calculated positions using a riding model with their U_{iso} values constrained to 1.5 times the U_{eq} of their pivot atoms for terminal sp^3 carbon atoms and 1.2 times for all other carbon atoms.

The compound is stable, and it retains the same orthorhombic crystal structure in the 110–373 K temperature range.

For all temperatures, very good residual parameters were obtained; smooth changes can be observed as a function of temperature. In particular, cell volume and anisotropic thermal displacement parameters linearly decrease when cooling down, while atomic positions change only slightly.

Crystallographic data for the structure at RT (see Tables S4 and S5, Supporting Information) have been deposited in the Cambridge Crystallographic Data Centre;[56] the .cif files for the other investigated temperatures are provided as Supporting Material.

[CSD-2 374 339 contains the supplementary crystallographic data for this paper. These data can be obtained free of charge from The Cambridge Crystallographic Data Centre via www.ccdc.cam.ac.UK/data_request/cif.]

Powder XRD Characterization and Analysis: XRD patterns were recorded on a Malvern-PANalytical 3rd generation Empyrean X-ray diffractometer, equipped with a 1.8 kW X-ray tube (CuK_α = 0.15406 nm) operating at 40 kV and 45 mA, W/Si elliptic focusing mirror, GaliPIX3D solid-state pixel area detector. The sample was sealed between two foils of 7 μm-thick Kapton lined with vacuum grease. The diffraction patterns were acquired at room temperature in transmission geometry and 1D mode using a transmission spinner sample stage (rotation speed = 2 rps). Whole-powder-pattern decomposition refinement based on the Pawley method was performed with HighScore Plus 5.2 to confirm the space group.

Mechanical Exfoliation and Deterministic All-Dry Viscoelastic Stamping: We exfoliated the bulk crystals inside a glovebox with Ar atmosphere, using scotch tape (Nitto blue tape, BT-150 E-KL). The flakes were then transferred to a piece of polydimethylsiloxane (PDMS, Gelfilm from Gelpak) and examined under an optical microscope (Nikon DS-Ri2). We stamped the selected flakes on Si/SiO_2 300 nm substrates by means of an all-dry viscoelastic stamping system,[57] which allows to place them deterministically, e.g., on top of pre-patterned contacts. XRD measurements were carried out using an Empyrean diffractometer (Malvern Panalytical) equipped with a Cu cathode on exfoliated flakes fully covering a Si/SiO_2 substrate.

Raman Spectroscopy and PL Measurements: Raman spectroscopy and PL measurements were performed with a Renishaw inVia Qontor micro-Raman instrument with a 50× objective, using a laser of 532 nm for Raman, and a laser of 405 nm for PL as excitation source, and a diffraction grating of 2400 lines/mm. Angle-resolved micro-Raman measurements were done placing the sample on a rotating piezoelectric motor (Thorlabs, ELL18/M rotation stage) controlled by the ELLO software. A half-wavelength plate (HWP) (Renishaw) was added to the optical path of excitation to achieve vertical (V) or horizontal (H) linear polarized light, with respect to the polarizer set at V at the detection path, so that a parallel or perpendicular configuration can be set. For collecting temperature-dependent spectra, we put the samples into a Linkam vacuum chamber

(10^{-6} hPa) cooled by liquid N_2, which allows to measure in the range 80–300 K. A 50× objective (Nikon, WD 11 mm, N.A. 0.60) was used to focus the laser on the sample, with a spot size of 1 μm. Python codes and the Wire 5.4 (Renishaw) software were used to analyze the data.

For measurements at low Raman shift (30–200 cm^{-1}), we used a Renishaw inVia micro-Raman instrument, equipped with an edge filter at 30 cm^{-1}, using a 532 nm laser as excitation source, a diffraction grating of 3000 lines/mm, and a 50× long distance objective. Angle-dependent linearly polarized measurements were obtained with the similar set up as described above (Thorlabs, ELL18/M rotation stage—PC controlled by ELLO software, laser polarization controlled by a HWP and a fixed polarizer at the spectrometer for parallel and perpendicular configurations).

Polarized-Resolved Optical Microscopy: Optical images with different polarization configurations were acquired with a Leica DM4000M microscope, using linear polarizers at the incidence and collection paths. Images were taken keeping the incident polarization fixed in the horizontal direction and rotating the polarizer at the collection path from 0° to 180°. Additionally, a rotating motorized stage was implemented, to rotate the sample while keeping the polarization fixed in the parallel or cross configuration.

Standard PL Lifetime Measurements: Samples were excited with a pulsed 375 nm laser (PicoQuant LDH-D-C-375, driven by a PDL 800-D controller, 40 MHz), which was focused down to a near-diffraction-limited spot. The PL was collected using a high numerical-aperture objective (Nikon CFI Plan Fluor, NA = 1.3), and the excitation laser was filtered out using a dichroic beamsplitter (SemRock FF376-Di01-25X36). The fluorescence was then projected onto an avalanche photodiode (APD, Micro Photon Devices PDM, 20 × 20 μm detector size). The laser and APD are synchronized using an electronic time-correlated single photon counting board (PicoHarp 300, a time-to-digital converter with a minimum time resolution of 4 ps).

Power-Dependent PL Measurements: Samples were excited using a 375 nm laser source (PicoQuant LDH-D-C-375) driven by a PDL 800-D controller and focused down to a near-diffraction limited excitation spot (≈500 nm FWHM) using a high numerical-aperture objective (Nikon CFI Plan Fluor, 100 X, NA = 1.3). The laser was operated in continuous wave (CW) mode, and the output power was adjusted manually by inserting a neutral density filter wheel (ThorLabs NDF) into the beam path. PL from the center of single crystalline flakes was collected using the same objective, and the excitation laser was filtered out using a dichroic beamsplitter (SemRock FF376-Di01-25X36). PL spectra were acquired using a Princeton Instruments SpectraPro HRS-300 imaging spectrograph coupled with an EMCCD camera (PI-MAX, Princeton Instruments). The PL (P_{out}) was extracted by the integration of the PL spectra collected.

Transient PL Microscopy: As described previously,[58,59] TPLM allows the extraction of the excitonic transport properties. The hybrid perovskitoid crystal was mechanically exfoliated using the scotch tape (Nitto Tape) method. After several exfoliation steps, the perovskite was transferred on a glass slide; flakes of ≈100 nm thick and several tens of microns in size were obtained. TPLM was subsequently performed by imaging through the glass slide with a 100x oil immersion objective (Nikon CFI Plan Fluor, NA = 1.3). TPLM uses a near-diffraction-limited exciton population generated using a 375 nm pulsed laser diode (PicoQuant LDH-D-C-375, PDL 800-D; 40 MHz, 7 μJ cm). The excitation laser was filtered out using a dichroic beamsplitter (SemRock FF376-Di01-25X36). The fluorescence emission was subsequently imaged with large magnification (330x) onto a scanning avalanche photodiode (APD, Micro Photon Devices PDM, 20 × 20 μm detector) to collect the emission from the exciton population. As a result, the demagnified image of the APD had an effective area of 60 × 60 nm (20 μm/330), which was scanned through the middle of the exciton population in 27 steps, recording a time trace in every point. The laser diode and APD were synchronized using a Pico-Harp 300 timing board for time-correlated single-photon counting. The time binning of the measurement setup was set to 4 ps.

Photocurrent Measurements: The sample was bonded with Al wire to a puck inside the Linkam chamber, electrically connected to a Keithley 2634B Source Meter. Measurements were taken under dark conditions and using a white lamp (its spectrum is available in Figure S10, Supporting Information) and 405 nm laser from the Raman instrument as illumination source, focused on the sample by a 50× objective. I(V)s were recorded in a computer using a LabVIEW program and I(t)s via a Python interface.

Statistical Analysis: All experimental data were collected from multiple independent samples (XRD: 2 powder samples, 2 single crystals, 2 exfoliated flakes; Raman spectroscopy: 2 flakes and 3 crystal samples per configuration; PL spectroscopy: 4 flakes and 5 crystal samples for temperature studies; Devices: 3 flakes). Data processing included background subtraction for Raman spectra (Renishaw WIRE v5.4). In Figure 4b, results are presented as mean values of three measurements with error bars representing standard deviation. All raw data were analyzed using Python 3.9.

Supporting Information

Supporting Information is available from the Wiley Online Library or from the author.

Acknowledgements

This work is supported under Projects PID2021-122511OB-I00 and PID2021-128004NB-C21 and under the María de Maeztu Units of Excellence Programme (grant CEX2020-001038-M) funded by Spanish MICIU/AEI/10.13039/501100011033 and by ERDF/EU. Additionally, this work was carried out with support from the Basque Science Foundation for Science (IKERBASQUE); concretely, B.M.G. thanks the IKERBASQUE project. L.O.V. thanks the funding from Spanish MICIU/AEI/10.13039/501100011033 and ESF+ for the PhD grant PRE2022-104385. D.S., B.M.-G., and M.G. thank support from the "Ramón y Cajal" Programme by the Spanish MICIU/AEI/10.13039/501100011033, European Union NextGenerationEU/PRTR and ESF+ (grant nos. RYC2022-037186-I, RYC2021-034836-I and RYC2021-031705-I, respectively). F.P. and A.C. thank funding from Spanish MICIU/AEI/10.13039/501100011033 (grant no. PID2022-141579OB-I00). D.S. and B.M.G. thank the Materials Department of IHP–Leibniz-Institut für innovative Mikroelektronik and Prof. C. Wenger for the access to the low-frequency Raman set-up during B.M.G. research stay. The authors thank R. Llopis for his support in the assembly of the Linkam vacuum chamber and Raman instrument optical polarization set-up motorization and implementation and Dr. E. Goiri Little for reading and revising the manuscript.

Conflict of Interest

The authors declare no conflict of interest.

Data Availability Statement

The data that support the findings of this study are available from the corresponding author upon reasonable request.

Keywords

exciton diffusions, hybrid organic–inorganic metal halides, low-dimensional materials, optoelectronics, photoluminescence, Raman spectroscopy

Received: April 9, 2025
Revised: June 4, 2025
Published online:

[1] X. Li, J. M. Hoffman, M. G. Kanatzidis, *Chem. Rev.* **2021**, *121*, 2230.
[2] Y. Asensio, L. Olano-Vegas, S. Mattioni, M. Gobbi, F. Casanova, L. E. Hueso, B. Martin-Garcia, *Mater. Horiz.* **2025**, *12*, 2414.

[3] Y. Han, S. Yue, B.-B. Cui, *Adv. Sci.* **2021**, *8*, 2004805.
[4] L. R. W. White, F. U. Kosasih, M. P. Sherburne, N. Mathews, S. Mhaisalkar, A. Bruno, *ACS Energy Lett.* **2024**, *9*, 835.
[5] X. Li, Y. He, M. Kepenekian, P. Guo, W. Ke, J. Even, C. Katan, C. C. Stoumpos, R. D. Schaller, M. G. Kanatzidis, *J. Am. Chem. Soc.* **2020**, *142*, 6625.
[6] Q. A. Akkerman, L. Manna, *ACS Energy Lett.* **2020**, *5*, 604.
[7] S. Sun, M. Lu, X. Gao, Z. Shi, X. Bai, W. W. Yu, Y. Zhang, *Adv. Sci.* **2021**, *8*, 2102689.
[8] Y. Zhao, H. Xiang, R. Ran, W. Zhou, W. Wang, Z. Shao, *J. Energy Chem.* **2023**, *83*, 189.
[9] H. Liu, T. B. Shonde, O. J. Olasupo, T. F. Manny, M. S. Islam, J. Viera, M. Khizr, S. Moslemi, X. Lin, J. S. R. V. Winfred, L. E. Nasser, *Adv. Mater.* **2024**, 2412239.
[10] J. Almutlaq, J. Yin, O. F. Mohammed, O. M. Bakr, *J. Phys. Chem. Lett.* **2018**, *9*, 4131.
[11] C. Zhou, L. Xu, S. Lee, H. Lin, B. Ma, *Adv. Opt. Mater.* **2021**, *9*, 2001766.
[12] P. S. Klee, Y. Hirano, D. B. Cordes, A. M. Z. Slawin, J. L. Payne, *Cryst. Growth Des.* **2022**, *22*, 3815.
[13] H. Hu, Y. Liu, Z. Xie, Z. Xiao, G. Niu, J. Tang, *Adv. Opt. Mater.* **2021**, *9*, 2101423.
[14] D.-Y. Li, Y.-H. Liu, Q. Wang, X.-W. Lei, C.-Y. Yue, Z.-H. Jing, *Mater. Today Chem.* **2023**, *31*, 101604.
[15] C. Sun, K. Jiang, M.-F. Han, M.-J. Liu, X.-K. Lian, Y.-X. Jiang, H.-S. Shi, C.-Y. Yue, X.-W. Lei, *J. Mater. Chem. C* **2020**, *8*, 11890.
[16] M. Mączka, D. Drozdowski, D. Stefańska, A. Gągor, *Inorg. Chem. Front.* **2023**, *10*, 7222.
[17] E. R. Dohner, A. Jaffe, L. R. Bradshaw, H. I. Karunadasa, *J. Am. Chem. Soc.* **2014**, *136*, 13154.
[18] S. Sahoo, R. Rana, S. L. Samal, *J. Solid State Chem.* **2025**, *341*, 125036.
[19] F. Fang, Y. Shen, Y. Li, K. Shih, H. Hu, H. Zhong, Y. Shi, T. T. Wu, *Small Science* **2025**, *5*, 2400443.
[20] Y.-Y. Wang, G.-H. Jia, M.-R. Huo, M.-T. Cheng, X.-Y. Chen, A.-R. Chang, J. Zhang, Y.-Y. Li, G.-M. Lin, *Inorg. Chem. Front.* **2024**, *11*, 5034.
[21] R. Azmi, S. Zhumagali, H. Bristow, S. Zhang, A. Yazmaciyan, A. R. Pininti, D. S. Utomo, A. S. Subbiah, S. De Wolf, *Adv. Mater.* **2024**, *36*, 2211317.
[22] J. H. Heo, J. K. Park, H. J. Lee, E. H. Shin, S. Y. Hong, K. Hong, F. Zhang, S. H. Im, *Adv. Mater.* **2024**, *36*, 2408387.
[23] M. Dong, B. Wang, Z. Yu, J. Zhao, X. Li, Y. Fu, Y. Guo, Y. Zhao, H. Gao, L. Jiang, Y. Wu, *Inorg. Chem. Front.* **2023**, *10*, 3396.
[24] H. Wang, S. Li, X. Liu, Z. Shi, X. Fang, J. He, *Adv. Mater.* **2021**, *33*, 2003309.
[25] D. Yang, B. Zhao, T. Yang, R. Lai, D. Lan, R. H. Friend, D. Di, *Adv. Funct. Mater.* **2022**, *32*, 2109495.
[26] T. Paul, S. Colella, E. Orgiu, *Appl. Phys. Rev.* **2024**, *11*, 041308.
[27] M. Maniadi, N. Mercier, C. Botta, V. Dupray, A. Abhervé, *Cryst. Growth Des.* **2025**, *25*, 2128.
[28] Y. Liu, H. Zhou, Y. Ni, J. Guo, R. Lu, C. Li, X. Guo, *Joule* **2023**, *7*, 1016.
[29] X. Li, W. Ke, B. Traoré, P. Guo, I. Hadar, M. Kepenekian, J. Even, C. Katan, C. C. Stoumpos, R. D. Schaller, M. G. Kanatzidis, *J. Am. Chem. Soc.* **2019**, *141*, 12880.
[30] K. Momma, F. Izumi, *J. Appl. Crystallogr.* **2011**, *44*, 1272.
[31] F. Faini, Y. Asensio, F. Visentin, L. Olano-Vegas, M. Hörmann, L. E. Hueso, G. Cerullo, F. V. A. Camargo, B. Martín-García, G. Grancini, *ACS Energy Lett.* **2025**, *10*, 120.
[32] D. Spirito, Y. Asensio, L. E. Hueso, B. Martín-García, *J. Phys. Mater.* **2022**, *5*, 034004.
[33] M. Shukla, *Polyhedron* **2016**, *105*, 200.
[34] B. Martín-García, D. Spirito, G. Biffi, S. Artyukhin, F. Bonaccorso, R. Krahne, *J. Phys. Chem. Lett.* **2021**, *12*, 280.
[35] A. M. A. Leguy, A. R. Goñi, J. M. Frost, J. Skelton, F. Brivio, X. Rodríguez-Martínez, O. J. Weber, A. Pallipurath, M. I. Alonso, M. Campoy-Quiles, M. T. Weller, J. Nelson, A. Walsh, P. R. F. Barnes, *Phys. Chem. Chem. Phys.* **2016**, *18*, 27051.
[36] D. Ghosh, D. Acharya, L. Pedesseau, C. Katan, J. Even, S. Tretiak, A. J. Neukirch, *J. Mater. Chem. A* **2020**, *8*, 22009.
[37] J. Yin, R. Naphade, P. Maity, L. Gutiérrez-Arzaluz, D. Almalawi, I. S. Roqan, J.-L. Brédas, O. M. Bakr, O. F. Mohammed, *Nat. Commun.* **2021**, *12*, 3995.
[38] V. J.-Y. Lim, M. Righetto, S. Yan, J. B. Patel, T. Siday, B. Putland, K. M. McCall, M. T. Sirtl, Y. Kominko, J. Peng, Q. Lin, T. Bein, M. Kovalenko, H. J. Snaith, M. B. Johnston, L. M. Herz, *ACS Energy Lett.* **2024**, *9*, 4127.
[39] S. N. Lavan, A. M. Sanni, A. S. Rury, Z.-F. Liu, *J. Phys. Chem. C* **2021**, *125*, 223.
[40] H. Abid, A. Trigui, A. Mlayah, E. K. Hlil, Y. Abid, *Results Phys.* **2012**, *2*, 71.
[41] S. Hou, Z. Guo, J. Yang, Y.-Y. Liu, W. Shen, C. Hu, S. Liu, H. Gu, Z. Wei, *Small* **2021**, *17*, 2100457.
[42] F. Wang, R. Lyu, H. Xu, G. Rui, B. Ding, *Responsive Mater.* **2024**, *2*, https://doi.org/10.1002/rpm.20240007.
[43] E. Zhang, P. Wang, Z. Li, H. Wang, C. Song, C. Huang, Z.-G. Chen, L. Yang, K. Zhang, S. Lu, W. Wang, S. Liu, H. Fang, X. Zhou, H. Yan, J. Zou, X. Wan, P. Zhou, W. Hu, F. Xiu, *ACS Nano* **2016**, *10*, 8067.
[44] S. Yang, C. Hu, M. Wu, W. Shen, S. Tongay, K. Wu, B. Wei, Z. Sun, C. Jiang, L. Huang, Z. Wang, *ACS Nano* **2018**, *12*, 8798.
[45] M. D. Smith, A. Jaffe, E. R. Dohner, A. M. Lindenberg, H. I. Karunadasa, *Chem. Sci.* **2017**, *8*, 4497.
[46] M. P. U. Haris, R. Bakthavatsalam, S. Shaikh, B. P. Kore, D. Moghe, R. G. Gonnade, D. D. Sarma, D. Kabra, J. Kundu, *Inorg. Chem.* **2018**, *57*, 13443.
[47] E. R. Dohner, E. T. Hoke, H. I. Karunadasa, *J. Am. Chem. Soc.* **2014**, *136*, 1718.
[48] H. Xiong, M. Wu, H. Zheng, B. Zhuang, Z. Tan, W. Yang, J. Fan, W. Li, *Adv. Opt. Mater.* **2024**, *12*, 2401199.
[49] E. Horváth, M. Spina, Z. Szekrényes, K. Kamarás, R. Gaal, D. Gachet, L. Forró, *Nano Lett.* **2014**, *14*, 6761.
[50] Z. Tan, Y. Wu, H. Hong, J. Yin, J. Zhang, L. Lin, M. Wang, X. Sun, L. Sun, Y. Huang, K. Liu, Z. Liu, H. Peng, *J. Am. Chem. Soc.* **2016**, *138*, 16612.
[51] Q. Fu, X. Wang, F. Liu, Y. Dong, Z. Liu, S. Zheng, A. Chaturvedi, J. Zhou, P. Hu, Z. Zhu, F. Bo, Y. Long, Z. Liu, *Small* **2019**, *15*, 1902890.
[52] SAINT, Bruker, V8.40B, Bruker AXS Inc., Madison, Wisconsin, USA., **2016**.
[53] L. Krause, R. Herbst-Irmer, G. M. Sheldrick, D. Stalke, *J. Appl. Crystallogr.* **2015**, *48*, 3.
[54] G. M. Sheldrick, *Acta Crystallogr. A Found Adv.* **2015**, *71*, 3.
[55] G. M. Sheldrick, *Acta Crystallogr. C Struct. Chem.* **2015**, *71*, 3.
[56] C. R. Groom, I. J. Bruno, M. P. Lightfoot, S. C. Ward, The Cambridge Structural Database, *Acta Crystallogr. B Struct. Sci. Cryst. Eng. Mater.* **2016**, *72*, 171.
[57] A. Castellanos-Gomez, M. Buscema, R. Molenaar, V. Singh, L. Janssen, H. S. J. van der Zant, G. A. Steele, *2D Mater.* **2014**, *1*, 011002.
[58] M. Seitz, A. J. Magdaleno, N. Alcázar-Cano, M. Meléndez, T. J. Lubbers, S. W. Walraven, S. Pakdel, E. Prada, R. Delgado-Buscalioni, F. Prins, *Nat. Commun.* **2020**, *11*, 2035.
[59] M. Seitz, M. Meléndez, P. York, D. A. Kurtz, A. J. Magdaleno, N. Alcázar-Cano, A. S. Kshirsagar, M. K. Gangishetty, R. Delgado-Buscalioni, D. N. Congreve, F. Prins, *ACS Energy Lett.* **2022**, *7*, 358.